Phase transition and high-pressure behavior of ulexite, a potential aggregate in radiation-shielding concretes

Davide Comboni[1*], Francesco Pagliaro[2], G. Diego Gatta[2], Paolo Lotti[2], Tommaso Battiston[2], Marco Merlini[2], Michael Hanfland[1]

[1] ESRF − European Synchrotron Radiation Facility, 71 Avenue des Martyrs, CS40220, 38043 Grenoble Cedex, France

[2] Dipartimento di Scienze della Terra, Università degli Studi di Milano, Via Botticelli 23, 20133 Milano, Italy

*** Corresponding Author:** Davide Comboni, current email address davide.comboni@esrf.fr

Abstract

The high-pressure behavior of ulexite [ideally $NaCaB_5O_6(OH)_6 \cdot 5(H_2O)$], a B-bearing raw material (with $B_2O_3 \approx 43$ wt%) and a potential B-rich aggregate, has been studied by in-situ single-crystal synchrotron X-ray diffraction up to 9.5 GPa, in order to explore its stability field at high pressure, the anisotropy of its compressional behavior and the deformation mechanisms at the atomic scale. Ulexite undergoes a first-order iso-symmetric phase transition, reconstructive in character, between 6.44 and 7.13 GPa (to the ulexite-II polymorph); the crystal structure of ulexite-II was successfully solved and refined. For the low-*P* polymorph of ulexite (stable in all the working conditions as aggregate in concretes), the isothermal bulk modulus here obtained is K_{V0} =36.9(5) GPa, with a strongly anisotropic compressional pattern (finite-Eulerian principal components of the unit-strain ellipsoid: $\varepsilon_1:\varepsilon_2:\varepsilon_3 \sim 7:3:1$). Ulexite-II also shows a marked anisotropic compressional pattern and with a resulting bulk softening (K_{V0} = 26(4) GPa).

Keywords: ulexite; crystal structure, elastic moduli, stability, phase transition

1. Introduction

Natural borates are the most important source of boron, an important geochemical marker (in particular in pegmatitic and granitic systems) for petrogenetic processes and a strategic element in a series of technological processes [1–4]. Highly concentrated, economically sized deposits of boron minerals, always in the form of borates, are relatively uncommon and unevenly distributed in the world usually in non-marine evaporites associated to hydrothermal activity [5]. Nowadays, such deposits are being exploited in Turkey, United States and several other countries [4]. Ulexite, often referred to as "TV rock" (due to its unusual optical features), is one of the most common borates and, alongside with kernite, borax and colemanite, account roughly for 90% of the borates used worldwide [5–7]. The 70% of the present reserves of boron ores is located in Turkey [4,6,8], where ulexite is profitably mined from the Bigadic and Kestelek deposits (Manisa province, Turkey) [9]. Furthermore, it occurs also in others deposits as secondary phase (*e.g.,* Emet and Kirka deposits in Turkey, and in the Tincalayu deposit and Sijes district, Argentina). Borates and boron-based materials are widely used in a number of applications: in heat-resistant pyrex and other low-thermal expansion glasses, in laundry bleaches and detergents, in flame retardants, as micronutrient in fertilizers, in some alloys and for many other purposes [4,10,11]. Notably, borates with a high content of B_2O_3, having relatively low cost and good abundance in nature (*e.g.*, kernite, colemanite, ulexite), are currently studied to assess their utilization as light aggregates in radiation-shielding materials. As a matter of fact, borates can act as neutron-shielding materials, due to the isotope ^{10}B (which accounts for about 20 % of natural boron) high cross section for thermal neutrons (~3840 barns) [12,13], leading to the reaction:

$$^{10}B + n \rightarrow \alpha + {}^{7}Li + \gamma \ .$$

Therefore, enhanced neutron radiation shielding capacity of protective structures can be achieved using cement-based composites with boron-containing aggregates (e.g., [14]). The use of borates alongside with other minerals as aggregates in concretes was also reported in order to attenuate γ-radiation [15–18]. Researchers have investigated the shielding and mechanical properties of borate-based aggregates in concretes, mortars and epoxy resins in order to enhance the shielding efficiency

towards neutron radiations [8,19–26]. Because of its low density (~2 g/cm^3) and cost, ulexite could be used for the production of concretes and a few studies have been devoted to determine the role of ulexite on the mortars and concretes properties (*e.g.*,[8,20]). However, a full and comprehensive characterization of the crystal-chemistry, elastic parameters, phase-stability and structural behavior (at the atomic scale) of ulexite, at varying *T* and *P* conditions, is still missing, and it would be advisable for modelling its thermo-mechanical properties when used as an aggregate, especially in neutron-shielding concretes [27–29]. The high-temperature behavior of ulexite, initially investigated by Stoch and Waclawaska, has more recently been studied by Sener et al. *via* , X-ray, IR, optical microscopy methods and TG, DTG and DTA analyses [30,31]. In the first stage of dehydration, completed at 118 °C, ulexite loses 1.5 mol of H_2O per unit cell but it retains its crystallinity up to 160°C, when the de-hydroxylation begins [31].

Recently, the behavior at non-ambient conditions of a series of natural borates has been studied, with the aim of improving the thermodynamic database of these minerals [32–40]. Overall, phase transitions occurring at different pressures were discovered in kernite, colemanite, kurnakovite and meyerhofferrite, which have structural homologies with ulexite. In particular, all these hydrated borates have several OH^- groups and H_2O molecules, making possible (even likeable) the increase of coordination of the Na-polyhedra and BO_3 groups in response to the applied pressure. On this basis, a phase transition at high-pressure, also in the case of ulexite, is not only possible but rather probable. For these reasons, the high-pressure behavior of ulexite has been investigated by *in-situ* single-crystal X-ray diffraction (up to 9.5 GPa) under hydrostatic conditions with the specific aim of: 1) modelling the *P-V* data in order to obtain the compressibility parameters (*i.e.*, in the form of axial and volumetric bulk moduli), which are currently unavailable in the literature; 2) investigating the phase-stability field of ulexite at high pressure and 3) describing the high-pressure structural re-arrangement of ulexite at the atomic scale.

1.1 Crystal structure of ulexite

Ulexite has the following ideal chemical formula, unit-cell parameters and symmetry: $NaCaB_5O_6(OH)_6 \cdot 5(H_2O)$, a ~8.816 Å, b ~12.87 Å, c ~6.678 Å, α~90.4°, β~109.1°, γ~105.0°, Sp. Gr. $P\bar{1}$. The crystallographic features of ulexite have been studied for the first time by Murdoch [41] and later re-examined by Clark and Christ [42], who successfully indexed X-ray powder diffraction pattern. Later, Clark and Appleman [43] provided the complex structure model by single-crystal X-ray diffraction [44]. The crystal structure of ulexite contains three kinds of structural units: (i) Ca-coordination polyhedra, which share edges (similarly to the kernite-II polymorph, [37]), (ii) Na-coordination octahedral chains not directly connected to the Ca-chains, and (iii) pentaborate polyanions, which connect the aforementioned Na- and Ca- chains (Fig.1). The Ca- and Na-polyhedral chains run parallel to c, the fiber-axis optical direction, whereas on the *ab* plane the whole structure is kept together by a pervasive H-bonds network, which is expected to play a primary role on the crystal-structure stability. Ulexite, like most borates at ambient pressure (*i.e.*, kernite, colemanite, meyerhofferrite, kurnakovite), has boron in both trigonal planar (B2 and B5) and tetrahedral (B1, B3 and B4) coordination. The BO_x units are organized in $[B_5O_6(OH)_6]^{3-}$ isolated borate polyanions, related to the well-known pentaborate polyanion $[B_5O_6(OH)_4]^-$, by the addition of two hydroxyl groups to two opposite B-O triangles (Fig. 1) [43].

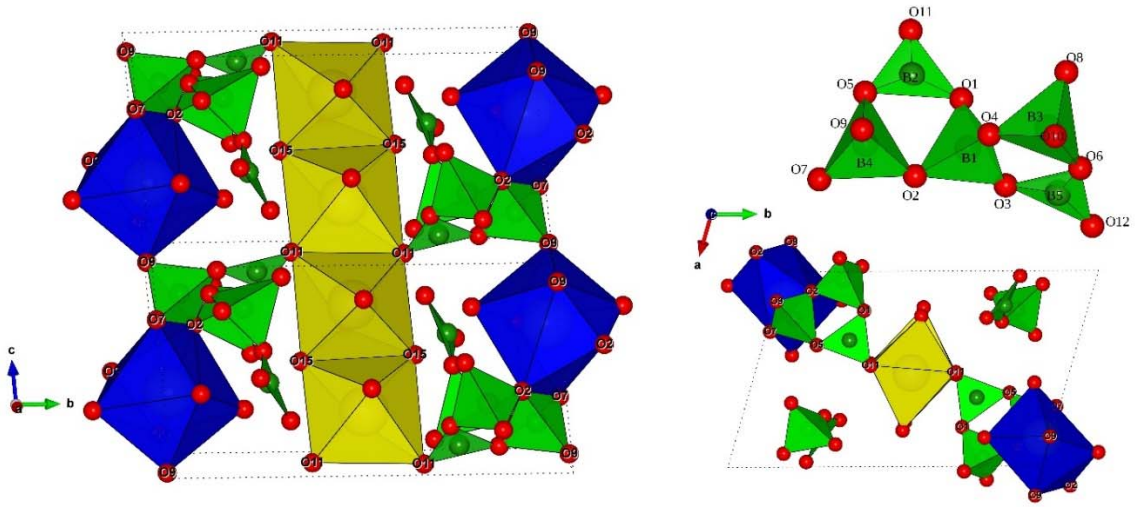

Fig1: Schematic representations of the principal structural units of ulexite at ambient pressure (Na-polyhedra in *yellow*, Ca-polyhedra in *blue,* BO_x groups in *green,* oxygen atoms in *red* spheres).

2. Experimental procedures

The sample of ulexite of this study was kindly provided by the Museum of Mineralogy - Earth Sciences Dept. University of Milan. Ulexite is a brittle and soft (2.5 in the Mohs scale) mineral with a perfect cleavage on the (010) and (110) crystallographic planes, generating acicular crystals, and it is soluble in hot water. Because of its crystal morphology, it was not possible to isolate a single crystal and, therefore, a poly-crystals sample with size ~ 8×4×3 μm^3 was selected for the X-ray diffraction experiment. An *in-situ* high-pressure single-crystal synchrotron X-ray diffraction experiment was performed at the ID15b beamline, at the ESRF, Grenoble (France). A convergent monochromatic beam (E~30 keV, λ~0.414 Å and ~200 mA) was used for the diffraction experiment. The diffraction patterns were collected by a MAR555 flat-panel detector, positioned at about 280 mm from the sample position. Sample-to-detector distance was calibrated using a Si standard and an enstatite ($MgSiO_3$) crystal. Further details on the beamline setup are reported in Merlini and Hanfland [45]. The poly-crystals sample (made by three individuals, one dominant and two subordinate) was loaded in a membrane-driven DAC, with 600 μm culet Boehler-Almax design anvils, along with a few ruby micro-spheres as pressure calibrant (pressure uncertainty ± 0.05 GPa, [46]). A stainless-steel foil (with thickness~250 μm) was pre-indented to 70 μm and then drilled by spark-erosion, leading to a *P*-chamber of ~300 μm in diameter. Since previous pilot experiments did not detect any relevant interaction between ulexite and an alcohol's medium, the conventional methanol:ethanol=4:1 mixture was used as hydrostatic *P*-transmitting fluid [47]. The adopted data collection strategy consisted in a pure ω-scan ($-32° \leq \omega \leq +32°$), with 0.5° step width and 0.25 s exposure time per step. High-pressure data were collected up to about 9.5 GPa. Indexing of the diffraction peaks and integration of their intensities (corrected for Lorentz-polarization effects) were performed using the CrysAlisPro package [48]. Corrections for X-ray absorption effects (caused by the DAC components) were applied using the semi-empirical ABSPACK routine implemented in CrysAlisPro [48]. All the structure refinements were performed using the package JANA2006 [49], in the space group $P\bar{1}$, using the initial fractional coordinates from Burns and Hawthorne [50]. As common for X-ray diffraction

experiments at high-pressure conditions, no H-sites were located and refined, due to the poor scattering value of H that hinders a reliable evaluation of displacement parameters and positions of the H-sites. To assess the reversibility of the detected phase transition and investigate its hysteresis, a few measures in decompression were taken. Selected diffraction patterns are shown in Fig. 2. The unit-cell parameters at high pressure are listed in Table 1 and their evolution with *P* is shown in Fig. 3.

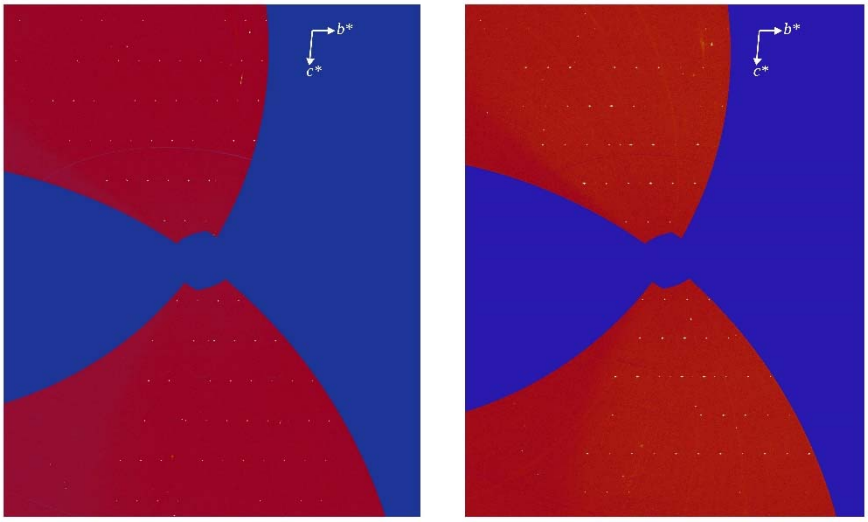

Fig.2: Reconstruction, based on the experimental data, of the *h0l** reciprocal lattice plane of ulexite- (*left side*) and ulexite-II (*right side*).

3.1. Structure refinement protocols

All the structure refinements were performed using the JANA2006 software [49]. For the low-pressure polymorph, the H-free structure reported by Burns and Hawthorne [50] was used as starting model. The displacement parameters (D.P.) of all sites were refined as isotropic (Table S1, Supplementary materials, SM). No restraints on bond distances or angles were used. Between 6.44(5) and 7.13(5) GPa, ulexite experienced an iso-symmetric phase transition, reconstructive in character, characterized by a 6% decrease in the unit-cell volume. Unfortunately, not all the datasets collected after the phase transition were refinable. At 7.13(5) GPa, the overall quality of the data was low. Repetitive data collections at this pressure were taken but no substantial progress was observed. At

8.20(5) GPa, two datasets were collected, one obtained rotating the DAC along the direction of the beam (and therefore parallel to the plane of the detector which is perpendicular to the direction of the beam) by roughly 60 degrees, in order to cover more reciprocal space. The two datasets so obtained were than simultaneously used by the *Superflip* software [51], implemented in JANA2006, to locate most of the crystallographic sites of the high-pressure polymorph of ulexite. A careful analysis of the difference-Fourier electron density maps allowed the location of the remaining missing atoms. This led to the solution of the structure of the high-pressure polymorph of ulexite, hereby referred to as ulexite-II, with reasonable statistical parameters (R_1 below 0.10). The obtained structural model was then used as starting point to refine also the datasets at 7.82(5) and 8.73(5) GPa. At 9.47(5) GPa, the hydrostatic limit of the methanol:ethanol pressure fluid was achieved and this prevented a good crystal structure refinement. The structure of ulexite-II is characterized by (static) atomic disorder and several sites were found to be only partially occupied. While the majority of sites involved in the Ca- and B1-, B2- and B4- polyhedra were found to have full site occupancy factors (*s.o.f.*), all the sites of the B3- and B5- tetrahedra, and a few of the Na-polyhedron, were found to be only partially occupied.

Table 1: Unit-cell parameters (*a, b, c, α, β, γ, V*) of ulexite with pressure (* data collected in decompression)

P(GPa)	*a*(Å)	*b*(Å)	*c*(Å)	*α*(°)	*β*(°)	*γ*(°)	*V*(Å^3)
0.0001	8.807(12)	12.867(7)	6.681(2)	90.31(4)	109.18(7)	105.24(11)	686(1)
0.03(5)	8.813(4)	12.863(4)	6.6706(8)	90.33(2)	109.10(2)	104.97(3)	686.9(4)
0.28(5)	8.776(3)	12.823(3)	6.6541(9)	90.32(2)	108.97(2)	105.13(3)	680.3(4)
0.69(5)	8.740(3)	12.768(3)	6.6276(6)	90.31(1)	108.71(2)	105.21(3)	672.7(3)
1.28(5)	8.678(3)	12.691(3)	6.5961(7)	90.30(1)	108.46(2)	105.47(3)	660.9(4)
1.55(5)	8.671(3)	12.668(3)	6.5812(7)	90.28(1)	108.30(2)	105.46(3)	658.4(3)
2.00(5)	8.632(3)	12.621(3)	6.5620(5)	90.25(1)	108.15(2)	105.65(3)	651.1(3)
2.57(5)	8.590(3)	12.570(2)	6.5406(6)	90.21(1)	107.96(2)	105.89(2)	643.1(3)
3.16(5)	8.567(3)	12.524(2)	6.5194(6)	90.17(1)	107.74(2)	106.03(2)	637.4(3)
3.73(5)	8.530(3)	12.476(2)	6.5002(5)	90.10(1)	107.56(2)	106.30(2)	630.2(3)
4.28(5)	8.493(3)	12.428(3)	6.4804(5)	90.03(1)	107.35(2)	106.59(3)	623.0(3)
5.00(5)	8.454(3)	12.366(3)	6.4580(7)	89.90(1)	107.11(2)	107.01(3)	614.4(3)
5.51(5)	8.431(3)	12.328(3)	6.4440(7)	89.79(2)	106.92(2)	107.30(3)	609.2(3)
6.44(5)	8.379(3)	12.260(3)	6.4252(7)	89.59(2)	106.71(2)	107.87(3)	599.3(3)
7.13(5)	8.489(4)	11.366(5)	6.471(2)	87.57(3)	108.17(3)	107.96(4)	563.3(4)
7.82(5)	8.431(3)	11.267(5)	6.4561(8)	88.25(2)	108.16(2)	107.47(3)	554.5(3)
8.20(5)	8.414(4)	11.247(6)	6.449(1)	88.42(3)	108.08(3)	107.51(4)	551.8(4)
8.34(5)	8.439(5)	11.196(7)	6.440(5)	88.43(9)	108.55(9)	107.67(6)	548.1(6)
8.73(5)	8.405(3)	11.196(2)	6.436(5)	88.20(1)	108.16(2)	107.66(2)	547.0(2)
9.47(5)	8.391(6)	11.136(8)	6.424(5)	88.34(9)	108.47(9)	107.80(6)	540.5(6)
6.45(5)*	8.511(6)	11.539(9)	6.456(6)	88.82(1)	108.2(1)	107.77(7)	571.7(8)
1.34(5)*	8.689(5)	12.667(7)	6.592(4)	90.42(8)	108.69(8)	105.50(5)	658.9(7)

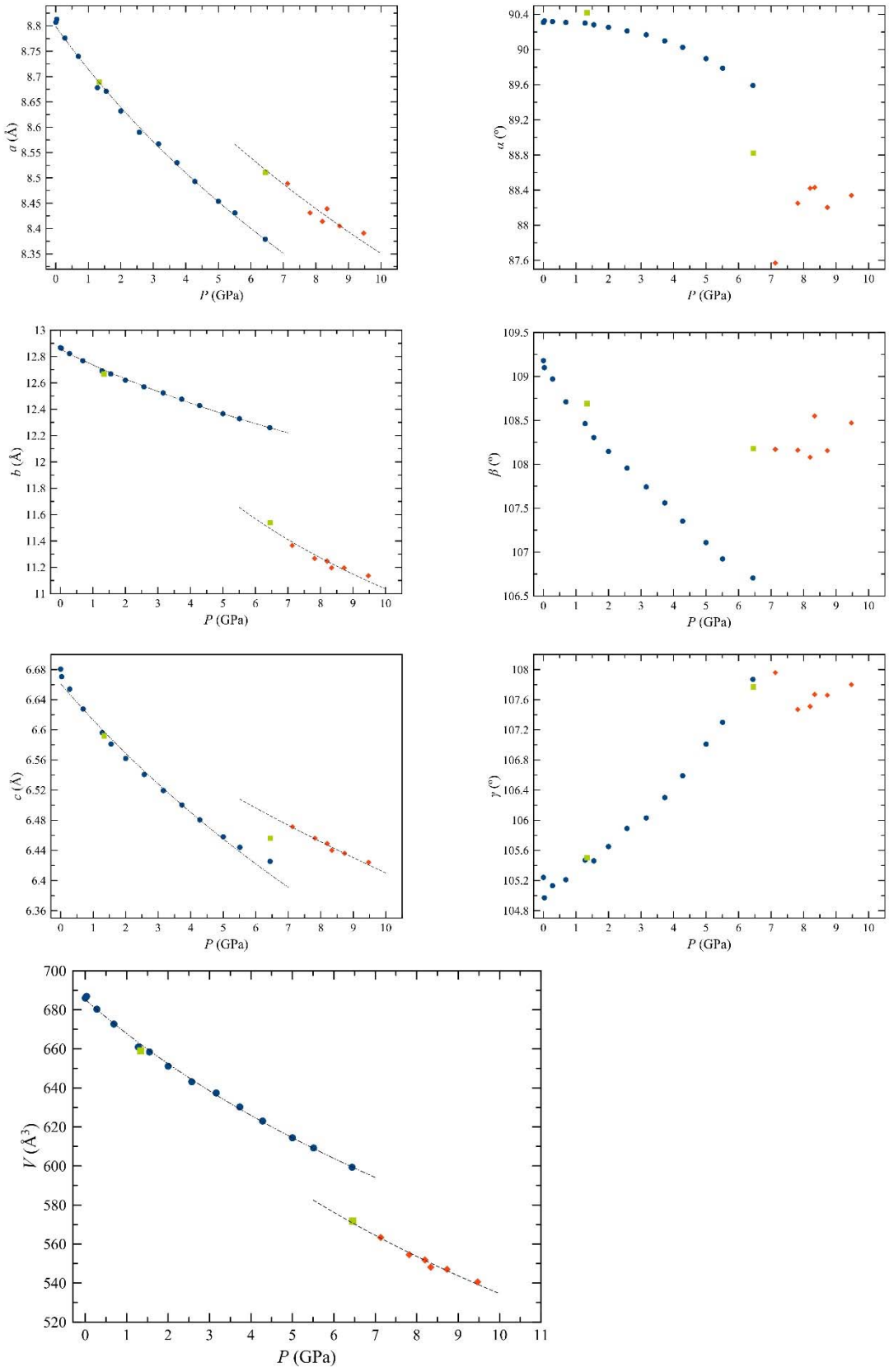

Fig.3: Evolution of the unit-cell parameters (*a, b, c, α, β, γ, V*) of ulexite. Low-pressure polymorph in *blue circles* and ulexite-II in *red diamonds*. The decompression path is displayed in *green squares.* The dashed lies represent the BM-EoS fits (see text for details).

Therefore, a few restrains were adopted. Into details, the sum of the *s.o.f.* of the split sites (B3a-b, B5a-b, Na_a-b, O3a-b, O6a-b, O8a-b, O10a-b, O12a-b, O15a-b and O17a-b) were forced to be equal to 1. Moreover, in order to decrease the number of refined parameters, only one (isotropic) displacement parameter (D.P.) was refined for each pair of split sites. It can be argued that the observed structural disorder could be due to a lowering of the symmetry (from $P\bar{1}$ to $P1$), coupled with a local topology change regarding the B3-, B5- and Na- polyhedra. Because of that, a pilot structure refinement was conducted in the $P1$ space group: no significant change was observed. Namely, the split sites displayed roughly the same *s.o.f.* with respect to the model refined in $P\bar{1}$. Very minor differences can be ascribed to the fact that the D.P. of all the oxygen sites was fixed to a given value in order to decrease the number of variables in the refinement. The structural changes pertaining to the ulexite-to-ulexite-II phase transition will be discussed in the next sections. Atomic coordinates, site occupancy factors and displacement parameters of the structure refinements of ulexite and ulexite-II are given in Table S1 (SM). The principal statistical parameters of the structure refinements are listed in Table S2 (SM). Inter-atomic angles and distances are reported in Tables 2 and 3a and 3b, respectively for ulexite-I and -II.

Table 2: B-O, Na-O and Ca-O distances (in Å) at different pressures in ulexite.

P (GPa)	Ca-O2	Ca-O2	Ca-O4	Ca-O7	Ca-O9	Ca-O9	Ca-O10	Ca-O13	Ca-O14
0.0001	2.51(2)	2.56(2)	2.39(2)	2.44(1)	2.57(1)	2.46(2)	3.34(3)	2.43(2)	2.39(3)
0.03(5)	2.50(1)	2.53(1)	2.40(1)	2.418(8)	2.594(9)	2.51(1)	3.34(2)	2.44(1)	2.42(2)
0.28(5)	2.50(1)	2.55(2)	2.38(1)	2.416(9)	2.58(1)	2.48(2)	3.31(2)	2.42(1)	2.35(2)
0.69(5)	2.49(1)	2.58(2)	2.40(1)	2.425(9)	2.56(1)	2.52(2)	3.31(2)	2.44(1)	2.36(2)
1.28(5)	2.46(1)	2.57(2)	2.38(1)	2.42(1)	2.55(1)	2.46(2)	3.29(2)	2.43(1)	2.40(2)
1.55(5)	2.45(1)	2.56(2)	2.38(1)	2.425(9)	2.54(1)	2.50(2)	3.28(2)	2.42(1)	2.38(2)
2.00(5)	2.44(1)	2.56(2)	2.36(1)	2.420(9)	2.52(1)	2.51(2)	3.28(2)	2.42(1)	2.39(2)
2.57(5)	2.42(1)	2.57(1)	2.36(1)	2.404(8)	2.515(9)	2.47(1)	3.27(2)	2.41(1)	2.34(2)
3.16(5)	2.41(1)	2.60(1)	2.34(1)	2.412(9)	2.498(9)	2.44(2)	3.25(2)	2.40(1)	2.34(2)
3.73(5)	2.41(1)	2.57(1)	2.34(1)	2.423(9)	2.49(1)	2.45(2)	3.24(2)	2.41(1)	2.35(2)
4.28(5)	2.39(1)	2.58(1)	2.34(1)	2.412(9)	2.48(1)	2.44(2)	3.24(2)	2.40(1)	2.34(2)
5.00(5)	2.38(1)	2.60(1)	2.33(1)	2.402(9)	2.47(1)	2.44(2)	3.20(2)	2.39(1)	2.35(2)
5.51(5)	2.37(1)	2.59(2)	2.35(1)	2.400(9)	2.47(1)	2.45(2)	3.19(2)	2.39(1)	2.33(2)
6.44(5)	2.35(1)	2.58(2)	2.31(1)	2.41(1)	2.47(1)	2.43(2)	3.18(2)	2.37(1)	2.34(2)

P (GPa)	Na-O1	Na-O11	Na-O11	Na-O15	Na-O15	Na-O16	Na-O17
0.0001	3.41(2)	2.42(2)	2.46(2)	2.46(2)	2.39(2)	2.41(3)	2.38(3)
0.03(5)	3.46(2)	2.42(2)	2.47(1)	2.47(1)	2.39(1)	2.36(3)	2.44(2)
0.28(5)	3.46(2)	2.42(2)	2.49(1)	2.46(1)	2.42(1)	2.37(3)	2.41(2)
0.69(5)	3.37(2)	2.40(2)	2.44(1)	2.44(1)	2.38(2)	2.43(3)	2.38(3)
1.28(5)	3.37(2)	2.39(2)	2.45(1)	2.43(1)	2.37(2)	2.36(3)	2.43(3)
1.55(5)	3.33(2)	2.37(2)	2.43(1)	2.43(1)	2.37(2)	2.37(3)	2.43(3)
2.00(5)	3.29(2)	2.37(2)	2.42(1)	2.42(1)	2.36(1)	2.35(3)	2.42(3)
2.57(5)	3.22(2)	2.34(1)	2.39(1)	2.41(1)	2.35(1)	2.32(2)	2.40(2)
3.16(5)	3.27(2)	2.34(2)	2.41(1)	2.40(1)	2.36(1)	2.34(3)	2.43(2)
3.73(5)	3.18(2)	2.32(2)	2.39(1)	2.41(1)	2.36(1)	2.35(3)	2.50(3)
4.28(5)	3.11(2)	2.32(2)	2.38(1)	2.38(1)	2.32(1)	2.35(3)	2.47(3)
5.00(5)	3.05(2)	2.30(2)	2.37(1)	2.37(1)	2.31(1)	2.32(3)	2.49(3)
5.51(5)	3.00(2)	2.29(2)	2.35(1)	2.37(1)	2.31(2)	2.35(3)	2.46(3)
6.44(5)	2.89(2)	2.28(2)	2.36(1)	2.37(1)	2.32(1)	2.32(3)	2.50(3)

P (GPa)	B1-O1	B1-O2	B1-O3	B1-O4	B2-O1	B2-O5	B2-O11	B3-O4	B3-O6
0.0001	1.56(3)	1.46(4)	1.49(2)	1.43(4)	1.38(4)	1.36(3)	1.38(3)	1.48(4)	1.49(2)
0.03(5)	1.50(2)	1.46(3)	1.46(2)	1.47(3)	1.35(3)	1.37(2)	1.43(2)	1.47(3)	1.49(1)
0.28(5)	1.48(2)	1.45(3)	1.48(2)	1.49(3)	1.35(3)	1.36(3)	1.37(2)	1.46(3)	1.48(2)
0.69(5)	1.44(2)	1.44(3)	1.50(2)	1.55(3)	1.39(3)	1.36(3)	1.35(2)	1.45(3)	1.50(2)
1.28(5)	1.44(2)	1.46(3)	1.47(2)	1.50(3)	1.39(4)	1.36(3)	1.31(2)	1.45(4)	1.49(2)
1.55(5)	1.45(2)	1.45(3)	1.48(2)	1.49(3)	1.38(3)	1.36(3)	1.34(2)	1.49(4)	1.49(2)
2.00(5)	1.43(2)	1.44(3)	1.50(2)	1.52(3)	1.40(3)	1.35(3)	1.31(2)	1.45(3)	1.50(2)
2.57(5)	1.50(2)	1.45(2)	1.48(2)	1.49(2)	1.36(3)	1.37(2)	1.36(2)	1.47(3)	1.47(1)
3.16(5)	1.43(2)	1.45(3)	1.49(2)	1.51(3)	1.35(3)	1.36(3)	1.39(2)	1.45(3)	1.49(1)
3.73(5)	1.50(2)	1.43(3)	1.47(2)	1.48(3)	1.34(3)	1.34(3)	1.37(2)	1.47(3)	1.48(1)
4.28(5)	1.44(2)	1.44(3)	1.49(2)	1.50(3)	1.34(3)	1.35(3)	1.34(2)	1.44(3)	1.49(2)
5.00(5)	1.42(2)	1.45(3)	1.49(2)	1.52(3)	1.34(3)	1.37(3)	1.36(2)	1.44(3)	1.49(2)
5.51(5)	1.43(2)	1.44(3)	1.49(2)	1.46(3)	1.37(3)	1.37(3)	1.36(2)	1.46(4)	1.50(2)
6.44(5)	1.53(2)	1.44(3)	1.47(2)	1.45(3)	1.31(3)	1.35(3)	1.37(2)	1.46(4)	1.48(2)

Table 3.a: Selected interatomic angles of the $[B_5O_6(OH)_6(H_2O)]^{3-}$ polyanions (see Section 4.1. Structure refinement protocol).

confA	O17-O6a-O10b	O17-O6a-O8	O3-O2-O7	O1-O4-O8
7.80(5) GPa	171.5(9)	123(1)	147.7(8)	83.9(6)
8.20(5) GPa	171(1)	124.2(9)	147.0(6)	83.7(5)
8.73(5) GPa	171(1)	126(2)	149(1)	84(1)

confB	O17b-O6b-O10b	O17b-O6b-O8b	O3b-O2-O7	O1-O4-O8b
7.80(5) GPa	173(2)	113.5(9)	156.0(8)	94.5(6)
8.20(5) GPa	173.2(9)	114.8(7)	156.1(6)	94.2(6)
8.73(5) GPa	177(1)	124(2)	158(1)	96.0(9)

Table 3.b: B-O, Na-O and Ca-O distances (in Å) at different pressures in ulexite-II in the two proposed configurations (see Section 4.1. Structure refinement protocol).

	7.80(5) GPa	8.20(5) GPa	8.73(5) GPa		7.80(5) GPa	8.20(5) GPa	8.73(5) GPa
Ca-O4	2.351(7)	2.324(8)	2.364(14)	Ca-O4	2.351(7)	2.324(8)	2.36(1)
Ca-O14	2.37(1)	2.33(1)	2.33(2)	Ca-O14	2.37(1)	2.33(1)	2.33(2)
Ca-O13	2.338(7)	2.339(8)	2.309(17)	Ca-O13	2.338(7)	2.339(8)	2.31(2)
Ca-O9	2.487(8)	2.409(8)	2.484(11)	Ca-O9	2.487(8)	2.409(8)	2.48(1)
Ca-O7	2.417(6)	2.415(6)	2.417(10)	Ca-O7	2.417(6)	2.415(6)	2.42(1)
Ca-O2	2.427(8)	2.416(7)	2.411(13)	Ca-O2	2.427(8)	2.416(7)	2.41(1)
Ca-O9	2.534(9)	2.478(6)	2.417(17)	Ca-O9	2.534(9)	2.478(6)	2.42(2)
Ca-O2	2.44(1)	2.545(9)	2.535(16)	Ca-O2	2.44(1)	2.545(9)	2.54(2)
Na_a-O1	2.35(1)	2.37(2)	2.35(2)	Na_b-O1	2.44(1)	2.43(2)	2.40(2)
Na_a-O3a	2.62(2)	2.58(2)	2.63(3)	Na_b-O11	2.67(1)	2.67(2)	2.61(2)
Na_a-O11	2.34(1)	2.35(1)	2.28(2)	Na_b-O16	2.38(1)	2.38(2)	2.39(2)
Na_a-O15a	2.45(3)	2.51(3)	2.48(6)	Na_b-O3b	2.57(2)	2.53(2)	2.61(4)
Na_a-O6a	2.43(3)	2.42(3)	2.39(5)	Na_b-O15b	2.32(3)	2.31(3)	2.32(4)
Na_a-O15a	2.62(3)	2.58(2)	2.58(5)	Na_b-O15b	2.21(3)	2.23(3)	2.24(6)
Na_a-O16	2.69(2)	2.67(2)	2.68(2)	Na_b-O17b	2.26(3)	2.31(3)	2.22(5)
Na_a-O17a	2.73(3)	2.71(3)	2.68(5)	Na_b-O6b	2.91(3)	2.95(3)	2.82(4)
B1-O4	1.45(2)	1.42(2)	1.50(3)	B1-O3b	1.43(2)	1.39(2)	1.41(3)
B1-O3a	1.51(2)	1.47(2)	1.50(2)	B1-O4	1.45(2)	1.42(2)	1.50(3)
B1-O1	1.47(1)	1.49(1)	1.42(2)	B1-O1	1.47(1)	1.49(1)	1.42(2)
B1-O2	1.48(2)	1.52(2)	1.52(2)	B1-O2	1.48(2)	1.52(2)	1.49(3)
B2-O1	1.37(2)	1.33(2)	1.37(3)	B2-O1	1.37(2)	1.33(2)	1.37(3)
B2-O5	1.36(1)	1.35(1)	1.35(3)	B2-O5	1.36(1)	1.35(1)	1.35(3)
B2-O11	1.33(1)	1.36(1)	1.34(2)	B2-O11	1.33(1)	1.36(1)	1.34(2)
B3a-O4	1.45(4)	1.45(3)	1.52(6)	B3b-O4	1.39(3)	1.39(3)	1.41(5)
B3a-O6a	1.43(3)	1.47(3)	1.41(4)	B3b-O6b	1.40(3)	1.39(2)	1.42(4)
B3a-O10a	1.47(5)	1.50(4)	1.44(7)	B3b-O10b	1.49(3)	1.48(2)	1.46(5)
B3a-O8a	1.64(3)	1.54(2)	1.49(4)	B3b-O8b	1.53(2)	1.53(2)	1.51(3)
B4-O2	1.50(1)	1.43(1)	1.49(3)	B4-O2	1.50(1)	1.43(1)	1.49(3)
B4-O5	1.44(1)	1.46(1)	1.43(2)	B4-O5	1.44(1)	1.46(1)	1.43(2)
B4-O7	1.44(2)	1.47(2)	1.45(3)	B4-O7	1.44(2)	1.47(2)	1.45(3)
B4-O9	1.51(2)	1.51(1)	1.50(3)	B4-O9	1.51(2)	1.51(1)	1.50(3)
B5a-O3a	1.48(5)	1.44(4)	1.43(7)	B5b-O3b	1.45(4)	1.38(4)	1.43(6)
B5a-O12a	1.42(3)	1.45(2)	1.50(4)	B5b-O17b	1.45(3)	1.46(3)	1.45(5)
B5a-O6a	1.41(5)	1.46(5)	1.32(7)	B5b-O12b	1.50(3)	1.48(2)	1.57(4)
B5a-O17a	1.55(2)	1.57(2)	1.52(4)	B5b-O6b	1.52(5)	1.54(4)	1.33(6)

3.2. Elasticity analysis

In order to describe the compressional behavior of ulexite, a Birch-Murnaghan Equation of State [52] (BM-EoS) was fitted to the experimental *P*-*V* data, using the EOS-FIT software [53]. This isothermal EoS assumes that the high-pressure strain energy in a solid can be expressed as a Taylor series in the Eulerian finite strain, defined as:

$$fe = [(V_0/V)^{2/3} - 1]/2.$$

The BM-EoS allows to refine the bulk modulus (K_{V0} or $K_{P0,T0}$ defined as $= -V_0(\partial P/\partial V)_{T0} = \beta^{-1}_{P0,T0}$, where $\beta_{P0,T0}$ is the volume compressibility coefficient at room conditions) and its *P*-derivatives ($K' = \partial K_{P0,T0}/\partial P$ and $K'' = \partial^2 K_{P0,T0}/\partial P^2$). When truncated to the second order in energy, $K' = \partial K_{P0,T0}/\partial P = 4$ and the EoS transforms to:

$$P(fe) = 3K_{P0,T0}\, fe\, (1 + 2fe)^{5/2}.$$

The truncation to the second-order in energy of the BM-EoS provided the best figure of merit for both the polymorphs of ulexite. The BM-EoS parameters, refined minimizing the difference between the EoS curve and the experimental data (weighted by their uncertainties in *P* and *V*), are listed in Table 4. Data were fitted taking into account an estimated uncertainty of ± 0.05 GPa for pressure [46].

Table 4: Refined elastic parameters pertaining to the different polymorphs of ulexite based on the isothermal II-BM Equation of State fits (*fixed parameter).

Ulexite	V_0, x_0 (Å^3, Å)	$K_{V0,\,x0}$ (GPa)	K'	$\beta_{V0,\,x0}$ (GPa^{-1})
V	685.2(6)	36.9(5)	4*	0.0271(4)
a	8.799(4)	32.7(7)	4*	0.0010(2)
b	12.855(4)	34.0(5)	4*	0.0098(1)
c	6.66(3)	44(1)	4*	0.0076(2)
				II-BM EoS, P< 6.44(5) GPa
Ulexite-II	V_0, x_0 (Å^3, Å)	$K_{V0,\,x0}$ (GPa)	K'	$\beta_{V0,\,x0}$ (GPa^{-1})
V	685(12)	26(4)	4*	0.038(5)
a	9.0 (2)	26(12)	4*	0.013(5)

b	12.9(3)	9(3)	4*	0.04(1)
c	6.67(2)	67(16)	4*	0.005(1)

II-BM EoS, P>6.44(5) GPa

4. Results and discussion

The results concerning the evolution of the unit-cell parameters with pressure, the deformation mechanisms at the atomic level and the resolution of the crystal structure of the high-pressure polymorph of ulexite (*i.e.*, ulexite-II) are described and discussed in the following sub-sections.

4.1 Compressional behavior

The evolution of the unit-cell parameters of ulexite with pressure (shown in Fig. 3 and listed in Table 1) appears to be monotonic up to 6.44(5) GPa, where a first-order phase transition (from ulexite to ulexite-II) occurs. Comparing the unit-cell volume of the low-*P* polymorph at 6.44(5) GPa and that of ulexite-II at 7.13(5) GPa, a difference of about 6% is observed. Interestingly, the ulexite-to-ulexite-II phase transition is characterized by an increase of the unit-cell edges length along the *a* and *c* crystallographic axes, respectively by about 1.3% and 0.7%, whereas the length decreases by about 7.3% along the *b* crystallographic axis. In the low-*P* polymorph, the α and *β* angles progressively decrease, respectively, from 90.3° and 109.18° at ambient pressure to 89.59° and 106.71° at 6.44(5) GPa. The angle *γ,* on the other hand, increases from 105.24° to 107.87° in the same *P*-range (Fig. 3, Table 1). Due to the phase transition, *α* decreases abruptly from 89.59° to 87.57°, whereas *β* increases from 106.71° to 108.17° (Fig. 3, Table 1). The evolution of the unit-cell parameters in decompression proves that the effects of the ulexite-to-ulexite-II phase transition are reversible (Fig. 3, Table 1). Ulexite is a relatively soft mineral, with a bulk modulus of 36.9(5) GPa; similar values were obtained for other borates (*e.g.*, kernite and meyerhofferrite, [37,39]). In ulexite-II, the bulk modulus decreases down to 24(3) GPa. Interestingly enough, the low-pressure polymorph of ulexite displays a modest anisotropic pattern, being the ratio between "linearized" bulk moduli along the three crystallographic axes: $K(a)_0$: $K(b)_0$: $K(c)_0$ ~ 1:1:1.35, but after the phase transition the anisotropic pattern becomes pronounced with $K(a)_0$: $K(b)_0$: $K(c)_0$ ~ 3:1:7.5 in ulexite-II (Table 4). This seems a rather abrupt change in the compressibility of ulexite. However, in a triclinic structure,

the unit-cell angles α, β, γ are free to change with pressure and a direct comparison of the values of the "linearized" (axial) bulk moduli of two polymorphs is not robust. In order to provide a comparative analysis of the anisotropic compressional patterns, magnitude and orientation of the Eulerian finite unit-strain (ε_l) ellipsoid for the two ulexite polymorphs were calculated, with the *Win_Strain* software [54]. The geometrical relationships between the strain ellipsoids and the principal crystallographic directions in ulexite and ulexite-II can be described by the following matrixes (with $\varepsilon_1>\varepsilon_2>\varepsilon_3$):

$$\begin{pmatrix}\varepsilon_1\\ \varepsilon_2\\ \varepsilon_3\end{pmatrix} = \begin{pmatrix}127(1)^\circ & 123(1)^\circ & 60.6(7)^\circ\\ 55.3(8)^\circ & 141(2)^\circ & 128(2)^\circ\\ 56(1)^\circ & 109(2)^\circ & 52(2)^\circ\end{pmatrix} \cdot \begin{pmatrix}a\\ b\\ c\end{pmatrix}$$

for ulexite between 0.0001 and 6.44(5) GPa, with $\varepsilon_1:\varepsilon_2:\varepsilon_3$ ~7:3:1, and

$$\begin{pmatrix}\varepsilon_1\\ \varepsilon_2\\ \varepsilon_3\end{pmatrix} = \begin{pmatrix}94(4)^\circ & 32(5)^\circ & 65(2)^\circ\\ 153(5)^\circ & 65(4)^\circ & 98(4)^\circ\\ 117(5)^\circ & 108(2)^\circ & 26(1)^\circ\end{pmatrix} \cdot \begin{pmatrix}a\\ b\\ c\end{pmatrix}$$

for ulexite-II between 7.13(5) and 9.47(5) GPa, with $\varepsilon_1:\varepsilon_2:\varepsilon_3$ ~7:4:1.

The results show that the ratio between the principal components of the unit-strain ellipsoid does not vary significantly between the two polymorphs. Nevertheless, there is a significant change on the orientation of the three principal directions of compression, which suggests that the deformation mechanisms at the atomic scale of the two polymorphs are rather different. Without the calculation of magnitude and orientation of the unit-strain ellipsoids for both the polymorphs, the compressibilities along the principal crystallographic axes would have led to a wrong description of the actual compressional anisotropy.

4.2. Phase transition and main deformation mechanisms

Up to 6.44(5) GPa, no dramatic change occurs in the crystal structure of ulexite. The B-O_x units are substantially uncompressible (as expected at low pressure). The only B-O distances that show an appreciable change are B2-O1 and B3-O10, which decrease by about 0.07Å and 0.1Å, within the mentioned *P*-range, leading to a distortion of these BO_x units. However, some relevant

modifications, regarding few inter-atomic distances of the B-, Na- and Ca- polyhedra, are critical in order to fully understand the deformation mechanisms that drive the ulexite-to-ulexite-II phase transition. Concerning the Na- and Ca-polyhedra, only the Na-O17 atomic distance increases considerably with pressure. O17 is the oxygen atom of a H_2O molecule bonded to the Na site. The second closest cation to O17 is B5, which is in triangular-planar coordination. At ambient pressure, Na-O17 is 2.38(2) Å, whereas at 6.44 GPa is 2.50(2) Å (see Table 2). This is coupled with the O17-approach to the B5 site: the B5-O17 distance is 3.45(3) Å and 3.11(3) Å respectively at ambient pressure and at a 6.44(5) GPa (see CIFs deposited). Between 6.44(5) and 7.13(5) GPa, ulexite undergoes a phase transition to ulexite-II. As previously mentioned, this is a first-order iso-symmetric phase transition, reconstructive in character, and the crystal structure of ulexite-II was successfully solved and refined. The phase transition is characterized by a sharp volume discontinuity of about 35 $Å^3$, and this is due to two main factors. First of all, B5 changes its coordination configuration from planar-triangular to tetrahedral, by bonding with the oxygen atom O17. This structural densification reflects the formation of isolated $[B_5O_6(OH)_6(H_2O)]^{3-}$ polyanions in substitution of the previous $[B_5O_6(OH)_6]^{3-}$ borate polyanions groups. Secondly, the phase transition induces a displacement of the Na-sites along the [100] crystallographic direction. This leads to an increase of the CN (coordination number) of Na from 6 to 7, by bonding with both O1 and O3 while losing one of the O11 sites (with which was bonded at low-pressure) (Fig. 4). The latter reconstructive mechanism is similar to what observed in the kernite-I-to-kernite-II phase transition [37] and shows some homologies also with other phase transitions of hydrated borates (e.g. colemanite and kurnakovite) [32,40]. At ambient pressure, one of the main structural factors of stability is the presence of continuous columns made by Na-octahedra in which each polyhedron shares an edge with the previous and the following polyhedra (connected by the O11 and O15 atoms) (Fig.1). The increase of the B5 coordination to tetrahedral, coupled with the Na migration, are likely the reasons for the decrease of axial compressibility along the [001] crystallographic direction (Fig. 4). After the phase transition, the Na-polyhedra do not form anymore continuous columns along the *c* direction but they are connected with

the B5 tetrahedra by sharing the O17 and O6 atoms. This increases the connection between the Na-groups and the borate polyanions, and could explain the lower compressibility of the ulexite-II polymorphs along the *c* edge (Fig. 4).

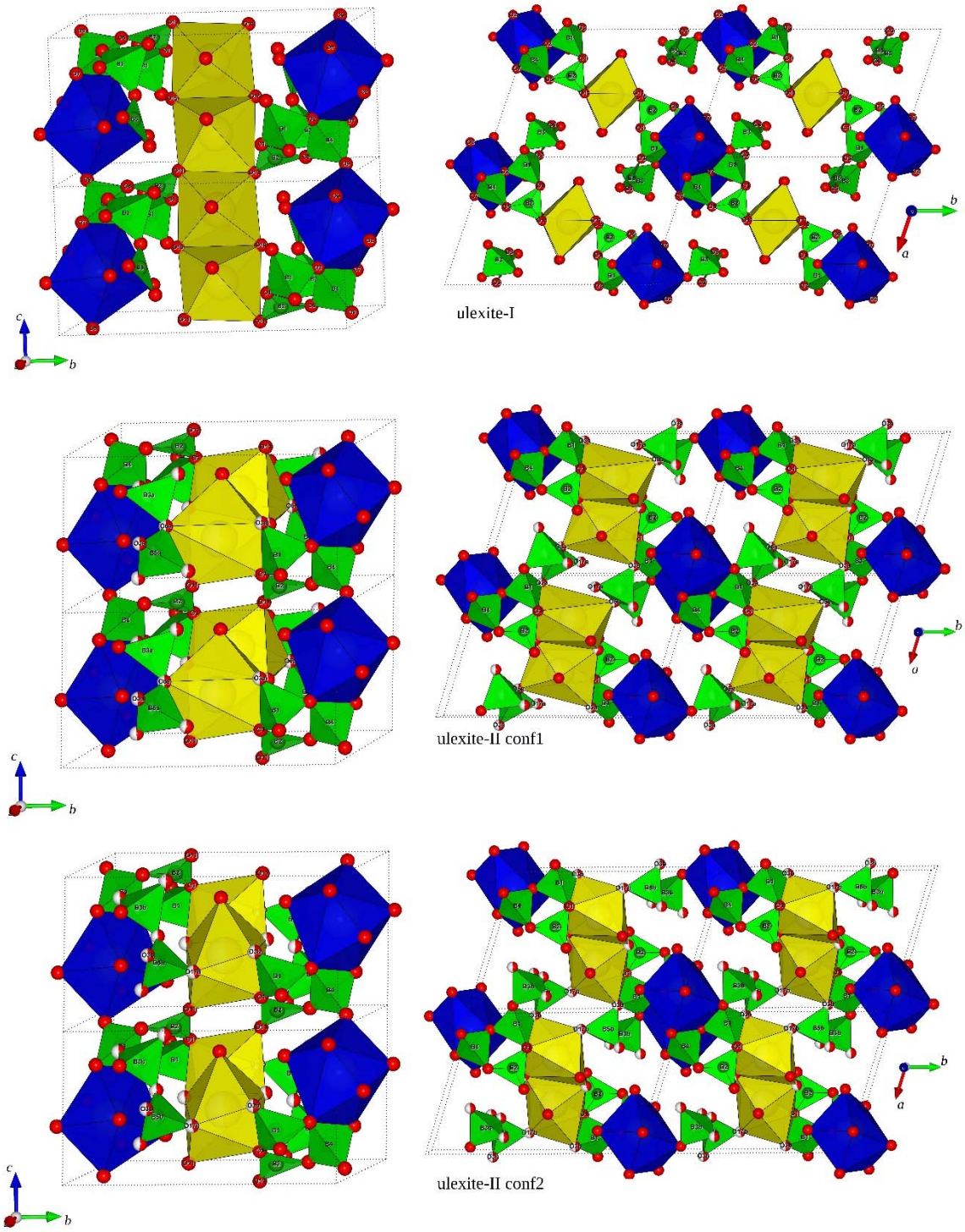

Fig.4: The crystal structure of ulexite viewed down [100] and [001]. From top to bottom: ulexite (low-*P* polymorph), ulexite-II configuration-*A,* ulexite-II second configuration-*B* (Na-polyhedra in *yellow*, Ca-polyhedra in *blue* and B-units in *green,* oxygen atoms in *red* spheres)

The Na-polyhedra columns are connected by the $[B_5O_6(OH)_6]^{3-}$ groups to the Ca-polyhedral chains, which also develop along the [001] crystallographic direction. However, in ulexite, the Na-polyhedra are connected to the $[B_5O_6(OH)_6]^{3-}$ groups by the O11 site, shared with B3 (which is in planar-triangular configuration). In ulexite-II, these linear columns are replaced by more complex building units. The migration of the Na-sites (manly along the [100] direction) generates units made by two Na-polyhedra per unit-cell, which are anymore not connected to the Na-polyhedra of the adjacent unit-cells along the [001] crystallographic direction (Fig. 4). The connection between the isolated Na-polyhedra pairs is provided by the borate polyanions $[B_5O_6(OH)_6(H_2O)]^{3-}$ groups.

4.3. Disorder and mutually exclusive configurations in the crystal structure of ulexite-II

With respect to other structures of borates investigated at high-pressure so far, a unique feature shown by the ulexite-to-ulexite-II phase transition is the occurrence of a marked structural disorder that mainly affects the B3 and B5 tetrahedra. The high-pressure phase transition induces the split of several sites, including B3, B5 and Na, in two half-occupied and mutually exclusive sites (see Table S1). Consistently, the oxygen atoms O3, O6, O8, O10, O12, O15 and O17 also split in partially occupied sites (again, with *s.o.f.* around 0.5). As previously explained in the **Section 3.1**, this could be related to a decrease of the ulexite symmetry (from $P\bar{1}$ to $P1$), but the structure, even if refined in $P1$, maintains the same structural disorder. The disorder can be explained considering the coexistence of two mutually exclusive and slightly different configurations here labeled as "*A*" and "*B*" (CIF files are deposited with the suffixes _confA and _confB, to which the *a* or *b* suffixes have been added to the split sites). Consistently, the *A* and *B* configurations display only one split site for each pair and each configuration has physically reasonable cation-anion distances. In the *A* configuration, the link between the Na-polyhedra and the borate polyanions involves the O6a, O3a, O11 and O1 atoms, whereas in the *B* configuration the connection involves the O17b, O3b, O11 and O1 atoms (Fig. 4). This is due to the tilting of the B5a and B3a tetrahedra around the O6 oxygen hinge, which in turn decreases its distances to Na_a of about 0.2 Å with respect to the configuration-*B*. The differences

between the B-O distances in the *A* and *B* configurations are marginal if compared to the tilting of the B3 and B5 tetrahedra. Table 3b shows the main O-O-O angles in the complex borate polyanions $[B_5O_6(OH)_6(H_2O)]^{3-}$ groups in the two different configurations. As can be seen in Fig. 5, the differences between the *A* and *B* configurations are mainly due to the tilting of the BO_x units in the borate polyanions groups, which causes differences of about 10° in some angles (Table 3b). Interestingly enough, the Na-O distances, listed in Table 3, suggest that the coordination number of sodium in configuration-*A* could be higher than 7. Considering the refinement at 7.80(5) GPa, the seven shortest Na-O distances range between 2.34(1) and 2.69(3) Å with an average distance of 2.50(2). In the configuration-*B,* the seven shortest Na-O distances range between 2.21(3) and 2.67(1) Å with an average distance of 2.41(2) (Table 3a). The resulting Na-polyhedron volume, referred to the shortest seven bonds, is therefore considerably smaller in the configuration-*B* (~19.3 $Å^3$) with respect to configuration-*A* (~21.5 $Å^3$). However, in configuration-*A*, because of the tilting around the O6a oxygen hinge of the B3a and B5a tetrahedra, the Na_a-O17a distance is only 2.73(2) Å, a reasonable distance for a Na-O interaction though not so strong. On the contrary, in the *B* configuration the closest 8th oxygen atom is at a Na_b-O6b distance of 2.91(2) Å. Therefore, it may be more correct to consider the CN of Na as 7 + 1 in the configuration-*A*.

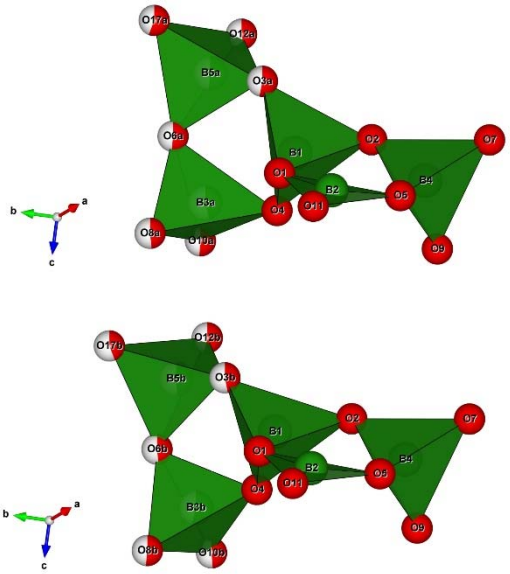

Fig.5: Representation of the borate polyanions $[B_5O_6(OH)_6(H_2O)]^{3-}$ group in ulexite-II (configuration-*A* top, configuration-*B* bottom).

The diagrams reported in Fig. 4 show a significant softening of the structure on the (001) plane, particularly along the [010] direction. However, apparently this has no clear justification. Fig. 4 shows the ulexite structure and the two configurations of ulexite-II viewed down [001] and [100]. On the *ab* plane, the structure seems to be more connected in ulexite-II than in ulexite. In ulexite-II,

the Na-polyhedra are connected with the $[B_5O_6(OH)_6(H_2O)]^{3-}$ groups *via* the O1, O3a and O6a oxygen hinges in configuration-*A* and O1, O3b and O17b in configuration-*B*. In ulexite, such connections do not take place and the structure has to rely on the hydrogen bond network. We cannot locate the H sites at high pressure and this prevents a robust discussion on the connections *via* the H-bonding network, the collapse of which could explain the sudden softening of the crystal structure, as observed in other materials [55]. We cannot exclude that the structural disorder, generated by the *P*-induced ulexite-to-ulexite-II phase transition, increases the compressibility of the structure because it destabilizes the H-bonding network, eventually producing the abrupt softening on the (001) crystallographic plane. Interestingly enough, the Ca-polyhedron seems not to be affected by the phase transition. If we compare the bond distances and the Ca-polyhedron volume at 6.44(5) GPa and after the phase transition, only minimal differences arise (Table 2 and 3). This can be easily explained taking in consideration what already observed in others borates at high pressure. In colemanite $[CaB_3O_4(OH)_3 \cdot H_2O]$, for example, the increase of the coordination of the Ca-polyhedron occurs only between ~14 and ~15 GPa and kurnakovite behaves similarly to colemanite, experiencing a phase transition between ~9 and ~11 GPa, with no change in the Mg-coordination number [33, 37]. In both kurnakovite and colemanite, only a fraction of trigonal-planar B increases its coordination from planar trigonal to tetrahedral by bonding with a H_2O-oxygen atom. In kernite $[Na_2B_4O_6(OH)_2 \cdot 3H_2O]$, on the other hand, the first high-pressure phase transition occurs already between ~1.6 and ~2.0 GPa. In that case, the main driving mechanism was the increase of the Na coordination number, from 6 to 7 (similarly to ulexite-II): two new bonds were generated and one was broken. This leads to the conclusion that, in the structure of hydrated borates, the Ca-polyhedra seem to be more stable with respect to the Na-polyhedra, probably due to the higher charge of the divalent Ca cation with respect to the monovalent Na, and this seems to be confirmed by the stable coordination environment of the divalent Mg at high-*P* in kurnakovite [37]. Consequently, high-pressure phase transitions that include changes in the coordination sphere of Ca-polyhedra (and possibly other divalent cations) are expected to occur at a higher pressure, with respect to phase transitions that affect Na-polyhedra. A confutation

of this could have been found in the structure solution of the meyerhofferite [$CaB_3O_3(OH)_5 \cdot H_2O$] high-pressure polymorph, that displays a phase transition at a relatively low pressure (between ~3.0 and ~3.5 GPa). Unfortunately, the crystal structure of the high-pressure polymorph of meyerhofferite has not been solved yet [39]. Overall, the phase transition occurring in ulexite is unique among the hydrated borates, because it is the only one that induces structural disorder. So far, ulexite is the hydrated borate in which the $B^{III} \rightarrow B^{IV}$ change of coordination has been observed to occur at the lowest pressure.

5. Summary and concluding remarks

In this study, we have investigated, for the first time, the high-pressure behavior of ulexite by *in-situ* single crystal X-ray diffraction, up to ~9.5 GPa. Data collected at high-pressure show that:

1. Ulexite is stable, in its ambient-conditions polymorph and with a fully-elastic compressional behavior, up to (at least) ~6.4 GPa. Between ~6.4 and ~7.1 GPa, ulexite undergoes a first-order iso-symmetric phase transition. The structure of ulexite-II has been successfully solved. The *P*-induced phase transition is reversible.
2. A marked structural disorder has been detected after the phase transition. Two coexisting and mutually exclusive configurations have been proposed, with physically consistent structural models.
3. One B site changes its coordination from planar-triangular to tetrahedral in response to the ulexite-to-ulexite-II phase transition. Furthermore, also the Na site increases its CN from 6 to (at least) 7. All the structural deformation mechanisms at the atomic scale, induced by the phase transition, have been here described.
4. The elastic parameters of the two ulexite polymorphs have been obtained. The polymorph stable at ambient conditions has an isothermal bulk modulus of ~44 GPa, which lies between those of other minerals usually used as aggregates, *e.g.* quartz (~37 GPa), as major components of sands, or calcite (~67 GPa), as major components of limestones, and it is

comparable to those of the main crystalline components of an ordinary Portland or Sorel cement, *e.g.* portlandite (~40 GPa) or brucite (~40 GPa). However, its compressional behavior is strongly anisotropic, with $\varepsilon_1:\varepsilon_3 \sim 7$. A significant change of the principal strain directions occurs in response to the *P*-induced phase transition from ulexite-to-ulexite-II.

It is worth mentioning that ulexite has a non-negligible content of Na_2O (~8 wt %), which could potentially be deleterious for the stability of Portland concrete because it promotes undesired reactions, undermining the durability of cements (*e.g.*, "alkali-silica reactions" – ASR). However, ASR can be promoted only under some given specific conditions, among those the high humidity at which the concrete is subjected, which can be easily avoided in shielding components of a nuclear-power plant. Furthermore, ulexite could be added in Sorel cements (*i.e.*, magnesium oxychloride cements), which are commonly used to make floor tiles and panels for fire protection. In this light, B-additivated Sorel cements could be efficiently used for the production of radiation-shielding tiles or panels.

Overall, this study improved the knowledge on the behavior of ulexite, adding new data: the pressure-stability range of ulexite far exceeds the working conditions of an aggregate in concretes or in other materials, and its elastic-compressional behaviour is adequate for an aggregate. Considering that service temperatures of radiation shielding structures in nuclear power plants can reach even 95 °C in localized hot-zones [29]), the main limitation to the use of ulexite in radiation-shielding concretes (made by Ca- or Mg-cement), as well as in mortars and epoxy resins, can be represented by its thermal stability and dehydration path. However, a partially dehydrated ulexite could work well. An additional open question concerns the solubility of ulexite in Portland paste (partially known [14]) or in Sorel paste (unknown) in the early hardening stage, and how the dissolution could be hindered. More experiments are, therefore, necessary.

Acknowledgements

ESRF is thanked for the allocation of the beamtime. GDG, FP, TB and PL acknowledge the support of the Italian Ministry of Education (MIUR) through the projects *"PRIN2017 - Mineral reactivity, a*

key to understand large-scale processes" (2017L83S77) and *"Dipartimenti di Eccellenza 2018–2022, Le Geoscienze per la Società: Risorse e loro evoluzione"*. GDG and PL acknowledge the support of the University of Milano through the project *"Piano di Sostegno alla Ricerca 2019"*.

References

[1] S. Barth, Application of boron isotopes for tracing sources of anthropogenic contamination in groundwater, Water Res. 32 (1998) 685–690. https://doi.org/10.1016/S0043-1354(97)00251-0.

[2] W.E. Seyfried, D.R. Janecky, M.J. Mottl, Alteration of the oceanic crust: Implications for geochemical cycles of lithium and boron, Geochim. Cosmochim. Acta. 48 (1984) 557–569. https://doi.org/10.1016/0016-7037(84)90284-9.

[3] J.M. Brenan, F.J. Ryerson, H.F. Shaw, The role of aqueous fluids in the slab-to-mantle transfer of boron, beryllium, and lithium during subduction: Experiments and models, Geochim. Cosmochim. Acta. 62 (1998) 3337–3347. https://doi.org/10.1016/S0016-7037(98)00224-5.

[4] W.G. Woods, An introduction to boron: History, sources, uses, and chemistry, Environ. Health Perspect. 102 (1994) 5–11. https://doi.org/10.2307/3431956.

[5] C. Helvacı, M.R. Palmer, Origin and distribution of evaporate borates- the primary economic sources of boron, Elements. 13 (2017) 249–254.

[6] USGS, Mineral Commodity Summaries 2020, 2020. https://www.usgs.gov/centers/nmic/mineral-commodity-summaries.

[7] R. Birsoy, Ü. Özbaş, Activity diagrams of borates: Implications on common deposits, Carbonates and Evaporites. 27 (2012) 71–85. https://doi.org/10.1007/s13146-012-0085-6.

[8] B. Oto, A. Gür, Determination of mass attenuation coefficients of concretes containing ulexite and ulexite concentrator waste, Ann. Nucl. Energy. 59 (2013) 72–74. https://doi.org/10.1016/j.anucene.2013.03.018.

[9] C. Helvaci, R.N. Alonso, Borate Deposits of Turkey and Argentina; A Summary and Geological Comparison, Turkish J. Earth Sci. 9 (2000) 1–27.

[10] S. Yu, X. Wang, H. Pang, R. Zhang, W. Song, D. Fu, T. Hayat, X. Wang, Boron nitride-based materials for the removal of pollutants from aqueous solutions: A review, Chem. Eng. J. 333 (2018) 343–360. https://doi.org/10.1016/j.cej.2017.09.163.

[11] S. Chen, L. Ai, T. Zhang, P. Liu, W. Liu, Y. Pan, D. Liu, Synthesis and application of a triazine derivative containing boron as flame retardant in epoxy resins, Arab. J. Chem. 13 (2020) 2982–2994. https://doi.org/10.1016/j.arabjc.2018.08.007.

[12] R.S. Carter, H. Palevsky, V.W. Myers, D.J. Hughes, Thermal neutron absorption cross sections of boron and gold, Phys. Rev. 92 (1953) 716–721. https://doi.org/10.1103/PhysRev.92.716.

[13] M. Palmer, G. Swihart, Boron isotope geochemistry: An overview, in: L. Anovitz, E. Grew (Eds.), Boron Mineral. Petrol. Geochemistry, Mineralogical Society of America, Washington, 1996: pp. 709–744.

[14] M.A. Glinicki, A. Antolik, M. Gawlicki, Evaluation of compatibility of neutron-shielding boron aggregates with Portland cement in mortar, Constr. Build. Mater. 164 (2018) 731–738. https://doi.org/10.1016/j.conbuildmat.2017.12.228.

[15] L.F. Amaral, G.C. Girondi Delaqua, M. Nicolite, M.T. Marvila, A.R.G. de Azevedo, J. Alexandre, C.M. Fontes Vieira, S.N. Monteiro, Eco-friendly mortars with addition of ornamental stone waste - A mathematical model approach for granulometric optimization, J. Clean. Prod. 248 (2020) 119283. https://doi.org/10.1016/j.jclepro.2019.119283.

[16] M.A. Khalaf, C.B. Cheah, M. Ramli, N.M. Ahmed, A. Al-Shwaiter, Effect of nano zinc oxide and silica on mechanical, fluid transport and radiation attenuation properties of steel furnace slag heavyweight concrete, Constr. Build. Mater. 274 (2021) 121785. https://doi.org/10.1016/j.conbuildmat.2020.121785.

[17] A.M. Zayed, M.A. Masoud, A.M. Rashad, A.M. El-Khayatt, K. Sakr, W.A. Kansouh, M.G. Shahien, Influence of heavyweight aggregates on the physico-mechanical and radiation attenuation properties of serpentine-based concrete, Constr. Build. Mater. 260 (2020) 120473. https://doi.org/10.1016/j.conbuildmat.2020.120473.

[18] M.T. Marvila, J. Alexandre, A.R.G. de Azevedo, E.B. Zanelato, Evaluation of the use of marble waste in hydrated lime cement mortar based, J. Mater. Cycles Waste Manag. 21 (2019) 1250–1261. https://doi.org/10.1007/s10163-019-00878-6.

[19] G. Guzel, O. Sivrikaya, H. Deveci, The use of colemanite and ulexite as novel fillers in epoxy composites: Influences on thermal and physico-mechanical properties, Compos. Part B Eng. 100 (2016) 1–9. https://doi.org/10.1016/j.compositesb.2016.06.054.

[20] T. Piotrowski, J. Glinicka, M.A. Glinicki, P. Prochoń, Influence of gadolinium oxide and ulexite on cement hydration and technical properties of mortars for neutron radiation shielding purposes, Constr. Build. Mater. 195 (2019) 583–589. https://doi.org/10.1016/j.conbuildmat.2018.11.076.

[21] K. Okuno, Neutron shielding material based on colemanite and epoxy resin, Radiat. Prot. Dosimetry. 115 (2005) 258–261. https://doi.org/10.1093/rpd/nci154.

[22] O. Gencel, W. Brostow, G. Martinez-Barrera, M.S. Gok, Mechanical properties of polymer concretes containing different amount of hematite or colemanite, Polimery/Polymers. 57 (2012) 276–283. https://doi.org/10.14314/polimery.2012.276.

[23] H. Binici, O. Aksogan, A.H. Sevinc, A. Kucukonder, Mechanical and radioactivity shielding performances of mortars made with colemanite, barite, ground basaltic pumice and ground blast furnace slag, Constr. Build. Mater. 50 (2014) 177–183. https://doi.org/10.1016/j.conbuildmat.2013.09.033.

[24] O. Aksołan, H. Binici, E. Ortlek, Durability of concrete made by partial replacement of fine aggregate by colemanite and barite and cement by ashes of corn stalk, wheat straw and sunflower stalk ashes, Constr. Build. Mater. 106 (2016) 253–263. https://doi.org/10.1016/j.conbuildmat.2015.12.102.

[25] N. Yildiz Yorgun, E. Kavaz, H.O. Tekin, M.I. Sayyed, F. Özdemir, Borax effect on gamma and neutron shielding features of lithium borate glasses: An experimental and Monte Carlo studies, Mater. Res. Express. 6 (2019). https://doi.org/10.1088/2053-1591/ab4fcc.

[26] M.F. Kaplan, Concrete radiation shielding : nuclear physics, concrete properties, design and construction, Longman Scientific & Technical, Harlow Essex England ;New York, 1989.

[27] M. Azenha, R. Faria, D. Ferreira, Identification of early-age concrete temperatures and strains:

Monitoring and numerical simulation, Cem. Concr. Compos. 31 (2009) 369–378. https://doi.org/10.1016/j.cemconcomp.2009.03.004.

[28] J. Domski, J. Katzer, An example of monitoring of early-age concrete temperatures in a massive concrete slab, Sel. Pract. Theor. Asp. Contemp. Mech. (2015) 94–105.

[29] J.. Torrenti, G. Nahas, Durability and Safety of Concrete Structures in the Nuclear ContextDurability and Safety of Concrete Structures in the Nuclear Context, in: Proceedingsof 6th Int. Conf. Concr. under Sev. Cond., Merida, Yucatan, 2010: pp. 3–18.

[30] L. Stoch, I. Waclawska, Thermal decomposition of ulexite, J. Therm. Anal. 36 (1990) 2045–2054. https://doi.org/10.1007/BF01914123.

[31] S. Sener, G. Ozbayoglu, S. Demirci, Changes in the structure of ulexite on heating, Thermochim. Acta. 362 (2000) 107–112.

[32] P. Lotti, D. Comboni, L. Gigli, L. Carlucci, E. Mossini, E. Macerata, M. Mariani, G.D. Gatta, Thermal stability and high-temperature behavior of the natural borate colemanite: An aggregate in radiation-shielding concretes, Constr. Build. Mater. 203 (2019) 679–686. https://doi.org/10.1016/j.conbuildmat.2019.01.123.

[33] G.D. Gatta, A. Guastoni, P. Lotti, G. Guastella, O. Fabelo, M.T. Fernandez-Diaz, A multi-methodological study of kernite, a mineral commodity of boron, Am. Mineral. (2020).

[34] G.D. Gatta, P. Vignola, Y. Lee, Stability of (Cs, K)$Al_4Be_5B_{11}O_{28}$ (londonite) at high pressure and high temperature: a potential neutron absorber material, Phys. Chem. Miner. 38 (2011) 429–434. https://doi.org/10.1007/s00269-011-0416-5.

[35] P. Lotti, G.D. Gatta, N. Demitri, G. Guastella, S. Rizzato, M.A. Ortenzi, F. Magrini, D. Comboni, A. Guastoni, M.T. Fernandez-Diaz, Crystal chemistry and temperature behavior of the natural hydrous borate colemanite, a mineral commodity of boron, Phys. Chem. Miner. 45 (2018). https://doi.org/10.1007/s00269-017-0929-7.

[36] P. Lotti, G.D. Gatta, D. Comboni, G. Guastella, M. Merlini, A. Guastoni, H.-P. Liermann, High-pressure behavior and P-induced phase transition of $CaB_3O_4(OH)_3 \cdot H_2O$(colemanite), J.

Am. Ceram. Soc. 100 (2017). https://doi.org/10.1111/jace.14730.

[37] D. Comboni, F. Pagliaro, G.D. Gatta, P. Lotti, S. Milani, M. Merlini, T. Battiston, K. Glazyrin, H. Liermann, High-pressure behavior and phase stability of $Na_2B_4O_6(OH)_2 \cdot 3H_2O$ (kernite), J. Am. Ceram. Soc. (2020) 1–11. https://doi.org/10.1111/jace.17185.

[38] G.D. Gatta, P. Lotti, D. Comboni, M. Merlini, P. Vignola, H.-P. Liermann, High-pressure behavior of $(Cs,K)Al_4Be_5B_{11}O_{28}$(londonite): A single-crystal synchrotron diffraction study up to 26 GPa, J. Am. Ceram. Soc. 100 (2017) 4893–4901. https://doi.org/10.1111/jace.14936.

[39] D. Comboni, F. Pagliaro, G.D. Gatta, P. Lotti, T. Battiston, G. Garbarino, M. Hanfland, High-pressure behaviour and phasestability of $Ca_2B_6O_6(OH)_{10} \cdot 2(H_2O)$(meyerhofferite), Phys. Chem. Miner. (2020). https://doi.org/10.1007/s00269-020-01117-3.

[40] F. Pagliaro, P. Lotti, T. Battiston, D. Comboni, G.D. Gatta, F.A. Camara, S. Milani, M. Merlini, K. Glazyrin, H. Liermann, Thermal and compressional behavior of the natural borate kurnakovite, $MgB_3O_3(OH)_5 \cdot 5H_2O$, Constr. Build. Mater. (2020). https://doi.org/10.1016/j.conbuildmat.2020.121094.

[41] J. Murdoch, Crystallography of ulexite, Am. Mineral. 25 (1940) 754–762.

[42] J. Clark, C. Christ, Studies of borate minerals (V): Reinvestigation of the X-ray crystallography of ulexite and probertite, Am. Mineral. 44 (1959) 712–719.

[43] J. Clark, D. Appleman, Pentaborate polyanion in crystal structure of ulexite $NaCaB_5O_6(OH)_6 \cdot 5H_2O$, Science (80-.). 145 (1964) 1295–1296. https://doi.org/10.1126/science.145.3638.1295.

[44] S. Ghose, Che'ng Wan, J.R. Clark, Ulexite, $NaCaB_5O_6(OH) \cdot 6H_2O$: structure refinement, polyanion configuration, hydrogen bonding, and fiber optics, Am. Mineral. 63 (1978) 160–171.

[45] M. Merlini, Marco; Hanfland, Single-crystal diffraction at megabar conditions by synchrotron radiation, High Press. Res. 33 (2013) 511–522.

[46] H.K. Mao, J. Xu, P.M. Bell, Calibration of the ruby pressure gauge to 800 kbar under quasi-hydrostatic conditions, J. Geophys. Res. 91 (1986) 4673.

https://doi.org/10.1029/JB091iB05p04673.

[47] S. Klotz, J.C. Chervin, P. Munsch, G. Le Marchand, Hydrostatic limits of 11 pressure transmitting media, J. Phys. D. Appl. Phys. 42 (2009). https://doi.org/10.1088/0022-3727/42/7/075413.

[48] Rigaku Oxford Diffraction, CrysAlisPro Software system, version 1.171.38.46., (2018).

[49] V. Petrícek, M. Dušek, L. Palatinus, Crystallographic computing system JANA2006: General features, Zeitschrift Fur Krist. 229 (2014) 345–352. https://doi.org/10.1515/zkri-2014-1737.

[50] P.C. Burns, F.C. Hawthorne, Hydrogen bonding in meyerhofferite: an X-ray and structure energy study, Can. Mineral. 31 (1993) 305–312. https://doi.org/10.3749/1499-1276-31.2.305.

[51] L. Palatinus, G. Chapuis, SUPERFLIP - A computer program for the solution of crystal structures by charge flipping in arbitrary dimensions, J. Appl. Crystallogr. 40 (2007) 786–790. https://doi.org/10.1107/S0021889807029238.

[52] F. Birch, Finite elastic strain of cubic crystals, Phys. Rev. 71 (1947) 809–824. https://doi.org/10.1136/bmj.1.4146.1034-b.

[53] R.J. Angel, J. Gonzalez-Platas, M. Alvaro, EosFit7c and a Fortran module (library) for equation of state calculations, Zeitschrift Fur Krist. 229 (2014) 405–419. https://doi.org/10.1515/zkri-2013-1711.

[54] R.J. Angel, Win_Strain. A program to calculate strain tensors from unit-cell parameters., (2011). http://www.rossangel.com/home.htm (accessed September 27, 1991).

[55] D. Comboni, G.D. Gatta, P. Lotti, M. Merlini, M. Hanfland, Anisotropic compressional behavior of ettringite, Cem. Concr. Res. 120 (2019) 46–51. https://doi.org/10.1016/j.cemconres.2019.03.012.